

Article

Effect of Friction Stir Welding on Short-Term Creep Response of Pure Titanium

Stefano Spigarelli ¹, Michael Regev ², Alberto Santoni ¹, Marcello Cabibbo ¹ and Eleonora Santecchia ^{1,*}

¹ Dipartimento di Ingegneria Industriale e Scienze Matematiche (DIISM), Università Politecnica Delle Marche, Via Brecce Bianche 12, 60131 Ancona, Italy; s.spigarelli@staff.univpm.it (S.S.); a.santoni@pm.univpm.it (A.S.); m.cabibbo@staff.univpm.it (M.C.)

² Mechanical Engineering Department, Braude College, P.O. Box 78, Karmiel 2161002, Israel; michaelr@braude.ac.il

* Correspondence: e.santecchia@staff.univpm.it

Abstract: Friction Stir Welding (FSW) is a recent joining technique that has received considerable attention. FSW causes significant variations in the material microstructure commonly associated with changes in the mechanical properties. The present study deals with the creep response of pure titanium (CP-Ti grade 2) after FSW. Dog-bone creep samples, obtained by machining, which show the longitudinal axis of each sample being perpendicular to the welding direction, were tested in constant load machines at 550 and 600 °C. The creep response of the FSW samples was analyzed and compared with that of the unwelded material. The shape of the creep curves was conventional, although the FSW samples went to rupture for strains lower than the base metal. The minimum creep rates for FSW samples were, in general, lower than for the unwelded metal tested in equivalent conditions. In addition, when the applied stress was high, deformation concentrated in the parent metal. The creep strain became more and more homogeneous along the gauge length as testing stress decreased. A constitutive model, recently developed for describing the creep response of the base metal, was then used to rationalize the observed reduction in the minimum strain rate in FSW samples.

Keywords: creep; titanium; friction stir welding; constitutive equations



Citation: Spigarelli, S.; Regev, M.; Santoni, A.; Cabibbo, M.; Santecchia, E. Effect of Friction Stir Welding on Short-Term Creep Response of Pure Titanium. *Metals* **2023**, *13*, 1616. <https://doi.org/10.3390/met13091616>

Academic Editor: Masahiro Fukumoto

Received: 22 August 2023
Revised: 14 September 2023
Accepted: 18 September 2023
Published: 19 September 2023



Copyright: © 2023 by the authors. Licensee MDPI, Basel, Switzerland. This article is an open access article distributed under the terms and conditions of the Creative Commons Attribution (CC BY) license (<https://creativecommons.org/licenses/by/4.0/>).

1. Introduction

Friction Stir Welding (FSW), a solid joining method that achieves a metallic bond below the melting point of the base material, is considered an attractive technology due to the absence of the metallurgical problems associated with the solidification process [1]. This property makes FSW particularly attractive when titanium and its alloys need to be joined since it avoids grain coarsening and the formation of oxides and pores [2–6] compared to fusion-based joining techniques. It is worth mentioning that while conventional welding tools can be used for FSW of stainless steel, Al, Mg, and Cu alloys, the high-melting temperature of Ti (1668 °C) requires the use of temperature-wear-resistant materials for the welding pin, such as tungsten-based materials (WC, WC-Co, and W-La) [7–11].

Moreover, being welding technology not based on fusion, FSW is considered a key technique for joining metals and alloys having a different nature and possibly a totally different chemical composition (i.e., Al- and Ti-based alloys) [12–16].

Commercially pure Titanium (Ti-CP) shows a combination of peculiar properties, such as yield strength comparable to austenitic stainless steel, which when combined with a great corrosion resistance performance, makes it a perfect candidate for a variety of applications, ranging from aerospace [17] and the chemical and petrochemical industry [18] to biomedical implants [19]. The presence of alloying elements are so low that the resulting Ti-CP has little response to heat treatment while enhancing the weldability of this alloy. However, oxygen content in the metal matrix can remarkably influence the mechanical properties of Ti-CP [20]. Nevertheless, when it comes to conventional welding technologies,

the combination of high temperatures and oxygen exposure can boost the O₂ pickup effect and lead to embrittlement of titanium-based matrix if the oxygen levels become very high [21,22].

Microstructures resulting from FSW are typically characterized by grain refinement, the intensity of which depends on the process parameters and the position considered inside the stir zone (SZ), as outlined by Fuji et al. [3], Kang and Lee [9]. Xu et al. [7] reported on grain refinement and twinning occurring on different locations of SZ, while Regev et al. [23] showed that the thermo-mechanically affected zone (TMAZ) is characterized by refined equiaxed grains due to dynamic recrystallization (DRX); moreover, both the stir zone and the TMAZ are affected by grain refinement and mechanical twinning.

A recent study [23] analyzed in detail the microstructures and the mechanical properties of FSW joints of commercially pure titanium (Ti-CP grade 2) sheets. In synthesis, the study confirmed that the thermo-mechanically affected zone (TMAZ) microstructure consists of refined equiaxed grains resulting from dynamic recrystallization (DRX). Grain refinement was also accompanied by extensive mechanical twinning in both the TMAZ and the stir zone (SZ). Although fracture had the same ductile nature in both unwelded metal and welded samples, tensile testing revealed that FSW resulted in a marked decrease in ductility.

The study, through its in-depth characterization of the FSW joints, was the basis for wider research aimed at investigating the effects of FSW on the creep of pure titanium. The creep response of titanium and its alloys has attracted great interest due to the many uses these materials have in industry [3,6,24–28]. Rosen and Rottem [25] showed that high-temperature exposure to air results in oxygen penetration at the surface of Ti-6Al-4V samples and has relevant implications on the final mechanical properties of this alloy. Ranganath and Mishra [26] compared the steady state creep behavior of pure Ti and compared it to Ti-Ti₂C and Ti-TiB-Ti₂C composites in the temperature range of 550–650 °C; the results showed that the creep rate of composites was two to three orders of magnitude lower than unreinforced Ti. Barboza et al. [27] analyzed the creep–fatigue failure mechanism and damage behavior of a Ti-6Al-3Nb-2Zr-1Mo titanium alloy at room temperature, showing that creep damage dominates the damage evolution in the initial stage, while in the later stages fatigue damage becomes predominant. Guo et al. [28] proposed a phenomenological creep–fatigue damage model that can be applied to the titanium alloy Ti-6Al-3Nb-2Zr-1Mo at room temperature and explain the stress dependence of the interaction between fatigue damage and creep damage. The model considered the influence that creep and fatigue damage can have on each other during room temperature exposition. In particular, while creep damage accumulates rapidly and dominates the damage progression in the early stages, fatigue damage is reported to dominate the later stages.

Nevertheless, no information is available on the effect of FSW on pure Ti. In addition, the availability of recent experimental data on the creep response of this pure metal remains another major issue. This led some of the authors of the present study to investigate the creep response in air of Ti-CP 2 at temperatures ranging from 550 to 650 °C [29]. Creep behavior of the base metal was shown to be strongly influenced by the growth of an oxygen-rich layer on the surface of the creep samples, during the high-temperature exposition inside the creep testing furnace. In fact, a direct relationship was found between the thickness and the hardness of the formed outer oxide layer, with the temperature level and the exposure time, or rather the higher the temperature, the higher the dwell time, and the higher the hardness of the surface oxide layer [29]. The present study represents a further step of this articulated research since it aims to investigate the creep response of the same material after FSW. All the details on the creep response of the unwelded material and the friction stir welded joints can be found in [23,29].

2. Materials and Methods

The base metal used in the present study was a Commercially Pure Ti–grade 2 (Ti-CP 2 in the following) with a UTS close to 500 MPa. Dog-bone creep cross-weld (CW) samples

were fabricated using the geometry illustrated in [23] ($3 \text{ mm} \times 3 \text{ mm}$ square section, 25 mm gauge length) and were creep-tested in constant load machines at 550 and 600 °C.

The optimal welding parameters were selected according to the criteria that have been thoroughly described in a previous paper published by some of the authors [23]. As a result, a rotational speed of 700 rpm and a transverse speed of 50 mm/min were chosen. Welding areas were subjected to visual inspection and radiographic characterization before samples were approved for further creep characterization and none of them showed defects within the stir zone of the weld.

All details about the quality, microstructure and properties of the CW samples can be found in [23]. As the notation CW indicates (Figure 1), the FSW direction was perpendicular to the longitudinal axis of the samples. To avoid the changes in the cross-sectional area evident in Figure 1, each sample was mechanically ground to obtain a regular thickness along the gauge length.

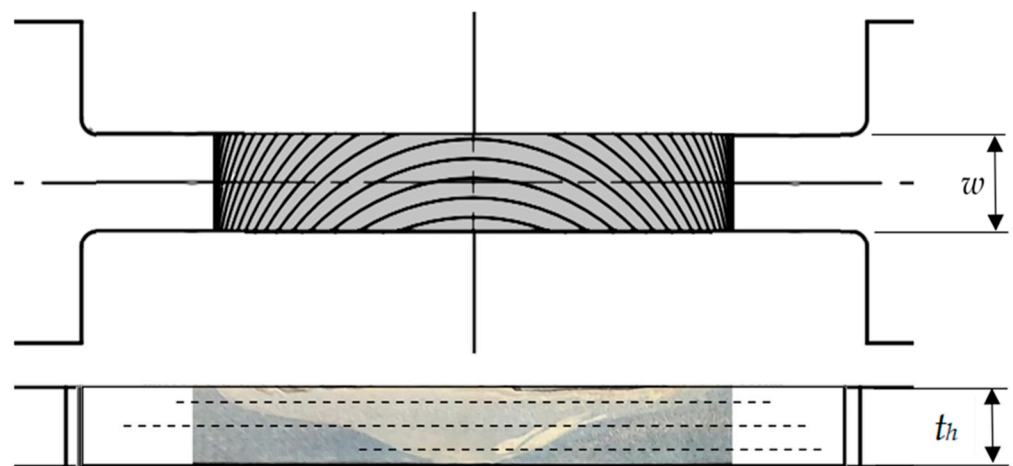


Figure 1. Schematic drawing of the dog-bone sample; in the front-view, the stir zone is marked in grey. The side view shows the macrostructure: the SZ is in light grey. The broken lines represent the portions of the sample, along the three horizontal profiles at different depths, where the Vickers microhardness HV was higher than 180 were measured (see [23] for full details on the microhardness results; Figure is here specular with respect to the pictures in [23], conforming with the thickness measurements in Figure 2).

Two types of experiments were carried out on the CW samples: seven constant-load creep experiments (CLE) and a single variable-load creep experiment (VLE). In CLEs, samples were subjected to 0.5 h soaking at the temperature of the test before the application of the defined load, maintained during the overall length of the test, which almost invariably corresponded to fracture. In the VLE, the sample was loaded after soaking, but the initial load was maintained until the minimum creep rate was reached and then increased.

Temperature was measured by four type-K thermocouples, three for furnace regulation, and the last for temperature recording. Elongation was continuously measured using LVDT. Creep experiments were carried out in the air. To avoid the effect of oxidation, well documented in the previous paper [29], the experimental load was purposely selected to obtain minimum creep rates above $1 \times 10^{-8} \text{ s}^{-1}$.

Optical microscopy investigations were performed using a Leica DMi8 (Leica Microsystems, Wetzlar, Germany) microscope; before the observations, samples were embedded in resin, mechanically ground, polished, and etched using Kroll's reagent (100 mL H_2O + 2 mL HF + 4 mL HNO_3).

3. Results

3.1. Mechanical Properties of the Joint

As mentioned above, the detailed analysis of the mechanical response (tensile curves and microhardness) for cross-weld samples was illustrated in [23]. A few pieces of crucial information from that study need to be recalled here. Figure 1 shows the schematic depiction of the cross-weld sample, redrawn to better appreciate the relative extensions of the different parts of the weld. As in [23], all the areas where heat and deformation occur will be identified with the notation TMAZ; therefore, SZ is included in the thermomechanically affected zone. Parent metal (PM), i.e., the part of the sample almost unaffected by FSW, forms the extreme portions of the gauge length. The side view of the sample in Figure 1 reports a macrograph, already discussed in [23], and three horizontal broken lines, each representing the part of the gauge length where the Vickers microhardness number HV was higher than 180 at that specific depth from the surface. Again, full details on the HV profile can be found in [23].

This simple analysis clearly demonstrates that a wide portion (80–85%) of the gauge length of the CW sample is formed by TMAZ with hardness well above 180 HV , the average value along the three lines in Figure 1 being 188 HV . The rest (15–20%) is formed by slightly deformed or undeformed PM, with an average microhardness of 166 HV . Thus, PM, in proximity to TMAZ, is just marginally harder than the Ti CP-2 sheets (150–160 HV).

Although a fully reliable relationship for estimating the UTS at room temperature (UTS_{RT}) from HV microhardness for pure Ti is still lacking, one could still profitably use the old equation obtained for Ti-based alloys [30]:

$$UTS_{RT} = 2.72 < HV + 96.5 \quad [\text{MPa}] \quad (1)$$

therefore providing the following values: $HV = 150, 166,$ and 188 (Ti-CP unwelded metal plates, PM, and TMAZ in the CW sample, respectively); and UTS values of 505, 553, and 608 MPa. The UTS at room temperature for the Ti-CP 2 plate [23] is correctly predicted by Equation (1).

Figure 2 plots two representative tensile curves for the Ti-CP 2 plates and the CW samples [23]. Let one assume that the CW sample is composed of two homogeneous zones, one (PM) much softer than the other (TMAZ), which deform independently under the same stress. This assumption is substantially correct since soft and hard fractions are stacked one above the other along the gauge length of the CW specimen. Then, the instantaneous increase in length L of the sample during the test is provided by

$$dL = dL_s + dL_h \quad (2)$$

where s and h denote the elongation of the soft and hard zones, respectively. After a few simple passages, one obtains the classical composite rule for the total strain:

$$\varepsilon = f_s \varepsilon_s + f_h \varepsilon_h \quad (3)$$

where f_h and f_s are the volume fraction of the hard and soft zone, respectively. Now, the TMAZ is stronger than the PM. The detailed microstructural analysis carried out in [23] demonstrated that FSW produces a deformed microstructure, characterized by very fine grains and extensive twinning. Such refined and deformed microstructures usually possess a high yield/ UTS ratio. Thus, let one suppose that the TMAZ deforms elastically during a tensile test. As a result, the total strain can be easily calculated as

$$\varepsilon = f_s \varepsilon_s + f_h \frac{\sigma}{E} \quad (4)$$

where ε_s for different stress values can be directly obtained by the tensile curve for pure Ti in Figure 2 (the difference in hardness between the PM portions of the CW samples and the Ti-CP 2 plate can be neglected here). Equation (4), with $f_h = 0.85$ and $f_s = 0.15$, provides

the model curve illustrated in Figure 2 (circles). The description of the tensile curve for the CW sample is excellent, at least until the onset of flow instability (necking). As predictable, the flow instability occurs when necking forms in the softer region (ϵ_s close to 0.3), which explains the substantially equivalent values of UTS_{RT} for the CW and pure Ti samples and the fact that fracture was invariably observed in PM.

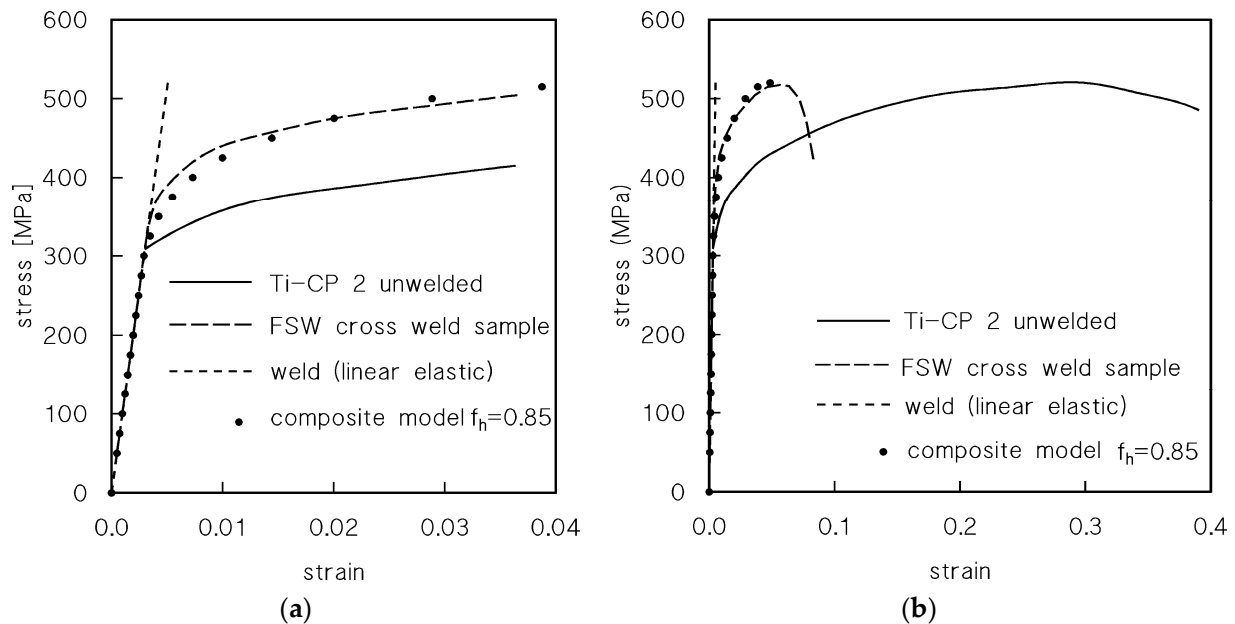


Figure 2. Representative tensile stress vs. engineering strain curves for the Ti-CP 2 and the FSW cross-weld samples (from [23]). Figure also plots the strain accumulated in the hard zone of the FSW sample ($HV > 180$), in the assumption that this portion of the specimen deforms elastically, and the resulting composite model curve (85% of the gauge length formed by the TMAZ with $HV > 180$): (a) initial part of the curves; (b) complete curves.

This simple analysis unambiguously demonstrates that in CW samples tested at room temperature, strain is mostly concentrated in the PM. A similar behavior should reasonably occur also at high temperatures, a problem which will be addressed further in the rest of the paper.

3.2. Creep Response

Figure 3 plots the strain rate vs. strain curves for CLEs and the single VLE of CW samples; as usual, the stress values are the nominal ones, i.e., they are calculated with reference to the initial area of the transversal section. The creep curves exhibited a conventional shape with a well-defined primary region, a minimum creep rate range, and a prolonged tertiary stage. The major difference with the creep curves observed by testing the samples with the same geometry machined from the Ti-CP 2 plate [29] is the lower elongation to fracture. In most cases, under high stresses, the CW samples ruptured at strains below 0.3, while the pure titanium samples accumulated higher deformation without visible damage. In addition, the minimum creep rates observed in most of the CW samples were lower than in the case of the titanium parent material sheet (Figures 4 and 5).

Figure 4 shows a direct comparison between the PM and CW curves obtained under the same nominal stress of 40 MPa. A general feature is the lowest strains to fracture of CW samples compared to the PM ones.

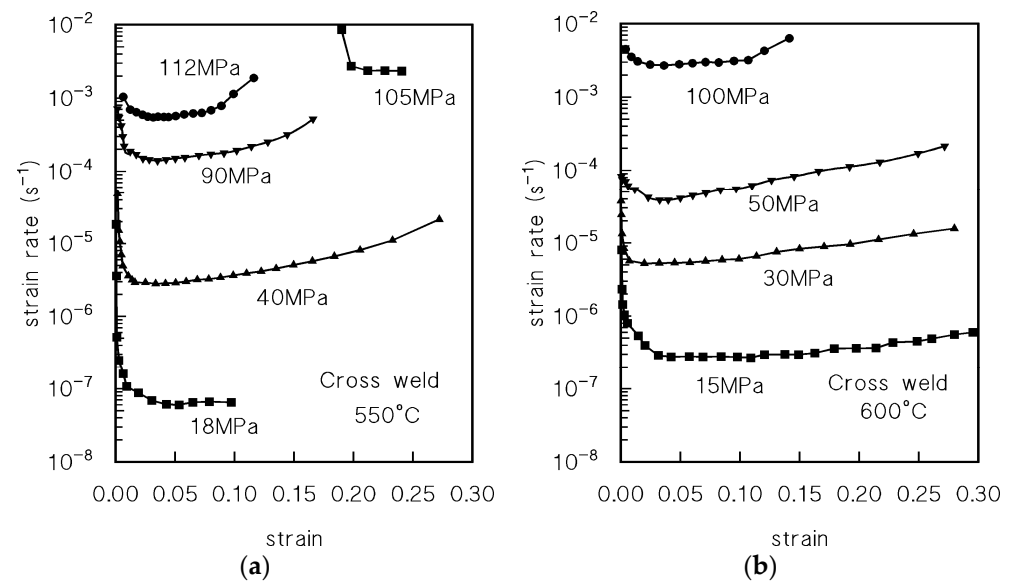


Figure 3. Strain rate vs. true strain creep curves in CW samples: (a) 550 °C; (b) 600 °C. In (a) the remarkable instantaneous plastic strain due to loading at 105 MPa (nominal) during the VLE, i.e., the separation between the two branches of the curve can be easily appreciated.

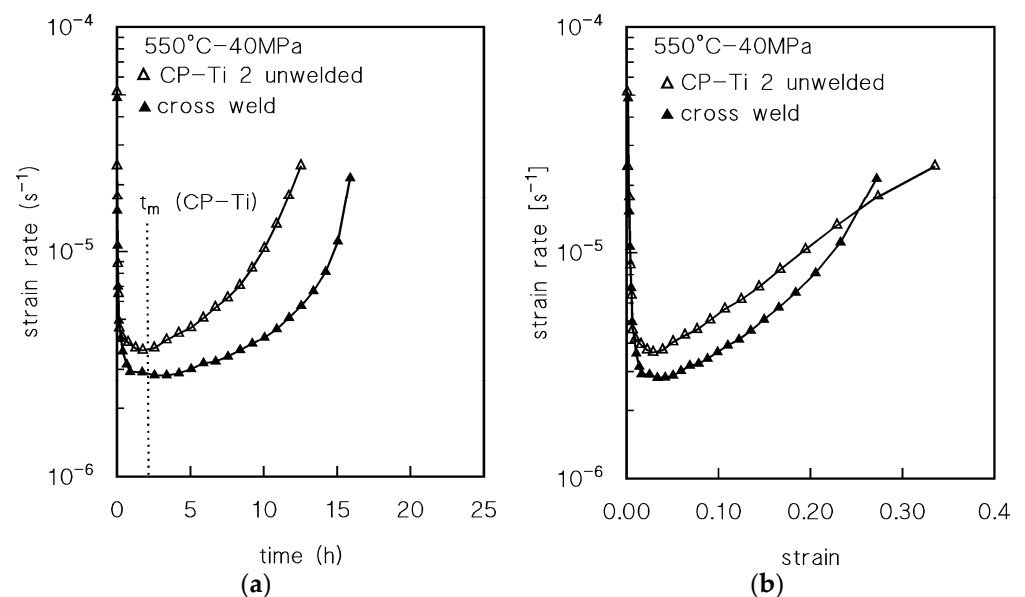


Figure 4. Comparison between the creep curves obtained by testing the parent material sheet (CP-Ti) under the same conditions and the cross-welded sample of the same material: (a) strain rate vs. time plot, (b) strain rate vs. strain plot. In (a) the time for minimum creep rate of CP-Ti sample is indicated by a dotted line.

In Figure 5, at both temperatures, the minimum creep rate data roughly align on straight slope lines close to 5.

Visual observation of the crept samples reveals that in creep, deformation is not homogeneous (Figures 6 and 7). Figure 6, in particular, shows a macrograph of the sample crept at 550 °C under 18 and 105 MPa (the VLE). The strain localization in the softer portions of the sample is apparent. Figure 7 shows the reduction in width (w) measured along half of the gauge length after creep (just half of the sample is considered since fracture occurred in most of the samples on the other side of the gauge length). The figure clearly suggests that when the sample is loaded under high stresses, strain is highly localized in PM, an effect that is much less pronounced in the low-stress region.

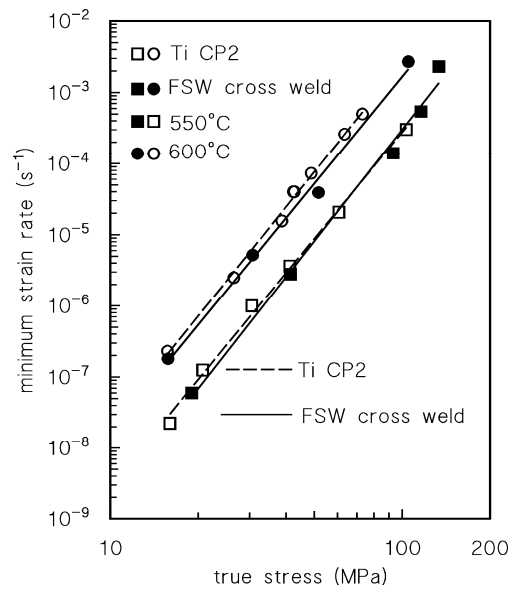


Figure 5. Minimum creep rate dependence on applied stress for Ti-CP 2 parent material and the FSW cross-weld samples of the same material.



Figure 6. Macrostructure of the sample tested at 550 °C-18/105 MPa. The variation in the sample thickness (t_h , see Figure 1) is evident.

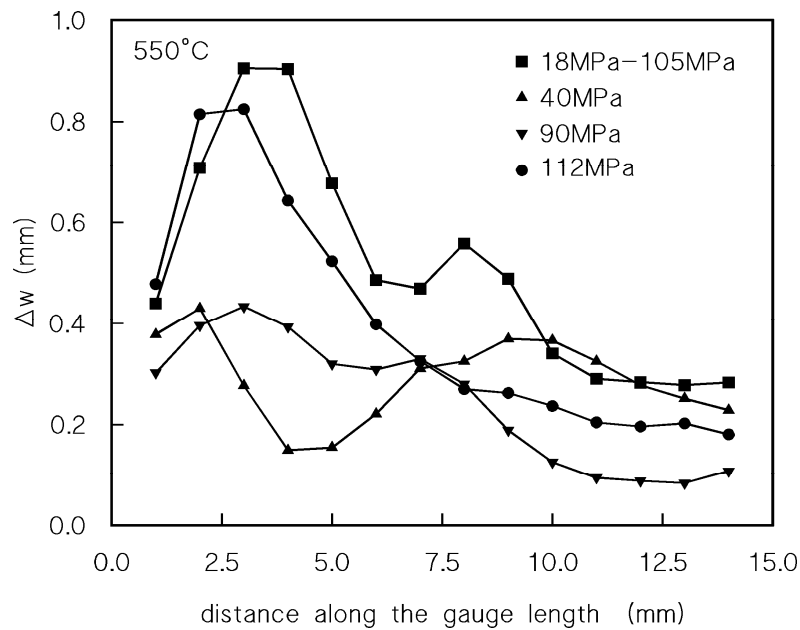


Figure 7. Reduction in sample width (w) along the gauge length measured after creep at 550 °C; only half of the gauge length was considered since in all cases—the only exception was the VLE under 18–105 MPa—the other half experienced fracture.

4. Discussion

A recent paper on the creep response of Ti CP 2 [29] demonstrated that an excellent description of the minimum creep rate ($\dot{\epsilon}_m$) dependence on applied stress (σ) and temperature (T) is provided by

$$\dot{\epsilon}_m = A \frac{D_{0L} G b}{kT} \left(\frac{\sigma}{G}\right)^3 \exp\left(\frac{\sigma b^3}{kT}\right) \exp\left\{-\frac{Q_L}{RT} \left[1 - \left(\frac{\sigma}{R_{max}}\right)^2\right]\right\}, \quad (5)$$

where $D_{0L} = 1 \times 10^{-8} \text{ m}^2\text{s}^{-1}$ and $Q_L = 193 \text{ kJ mol}^{-1}$ describe the self-diffusion in low-purity Ti [31], G is the shear modulus, b is the length of the Burgers vector ($2.95 \times 10^{-10} \text{ m}$), T is the absolute temperature, k is the Boltzmann constant, R is the gas constant, and $A = 50$. The R_{max} parameter was provided by

$$R_{max} = 2.8 UTS_T, \quad (6)$$

where UTS_T is the tensile strength at the testing temperature. Since Equations (5) and (6) work reasonably well for PM, they might be, in principle, also used to describe the minimum creep rate dependence on applied stress for the CW samples. As obvious, the complex macro- and microstructure of these components should be considered: let one suppose that, at the time corresponding to the time for minimum strain rate (t_m) for PM, the strain rate is very close to its minimum value for the material of the TMAZ. If such is the case, a derivation of Equation (3), at $t = tm$, provides, for a CW sample, the following:

$$\dot{\epsilon}_m \approx f_s \dot{\epsilon}_{ms} + f_h \dot{\epsilon}_{mh} \quad (7)$$

Figure 4 shows that at $t = tm$ for PM, the strain rate of the CW sample is indeed very close to the minimum, in agreement with Equation (7). The major point is the determination of the minimum creep rate dependence on applied stress and temperature for the hard (TMAZ) and soft (PM) zones. These are compositionally similar, but heat and deformation produce a hardened structure in TMAZ. On the other hand, the only input parameter required in Equation (5) is R_{max} , but UTS_T is available only for the virgin material [32]. These values of the high temperature (500–600 °C) UTS for Ti-CP 2, obtained from the curves presented in [5], were tentatively described by an equation in the form of

$$UTS_T = B UTS_{RT} \exp\left(\frac{Q_{UTS}}{RT}\right) \quad (8)$$

where B and Q_{UTS} are material constants. Figure 8 demonstrates that the UTS_T data at 500, 550, and 600 °C, once plotted as a function of $1/T$ in a semi-logarithmic plot, closely align on a straight line, which corresponds to $B = 1.4 \times 10^{-3}$ and $Q_{UTS} \approx 34 \text{ kJ mol}^{-1}$. Equation (8) can be then combined with Equation (1), providing

$$UTS_T = B(2.72HV + 96.5) \exp\left(\frac{Q_{UTS}}{RT}\right) \quad (9)$$

Equations (5), (6) and (9) provide, for CP-Ti 2 ($HV = 150$), the model curves for minimum creep rate dependence on applied stress and temperature shown in Figure 9 (broken lines). These curves are equivalent to those obtained in [29].

The same procedure can then be used to calculate the minimum creep rate dependence on applied stress for the two constituents of the CW samples, i.e., PM ($HV = 166$) and TMAZ ($HV = 188$), on the tacit assumption that B and Q_{UTS} do not vary. The resulting values of the minimum creep rate under a given stress for PM and TMAZ can be simply combined by Equation (7) (again with $f_s = 0.15$), obtaining the model curves illustrated in Figure 9 (solid lines). The description of the experimental data is very good. In addition, the model explains why deformation appears more and more homogeneous as stress decreases. The R_{max} parameter, which strongly depends on UTS , substantially affects the minimum

creep rate dependence on stress and temperature only in the high-stress regime. There, the model predicts that the creep rate for the harder TMAZ is much lower than for the softer PM, which thus deforms to a larger extent. Thus, the stress for obtaining a minimum creep rate of 10^{-4} s^{-1} at 550 and 600 °C is roughly 10 and 8.5% higher for the CW samples than for unwelded material. In the low-stress regime, where the effect of R_{max} becomes negligible, both PM and TMAZ should deform with essentially the same strain rate, leading to homogeneous deformation along the gauge length. In this case, the stress for a minimum creep rate of 10^{-6} s^{-1} at 550 and 600 °C is merely 4 and 2.5% higher for the CW samples than for unwelded material.

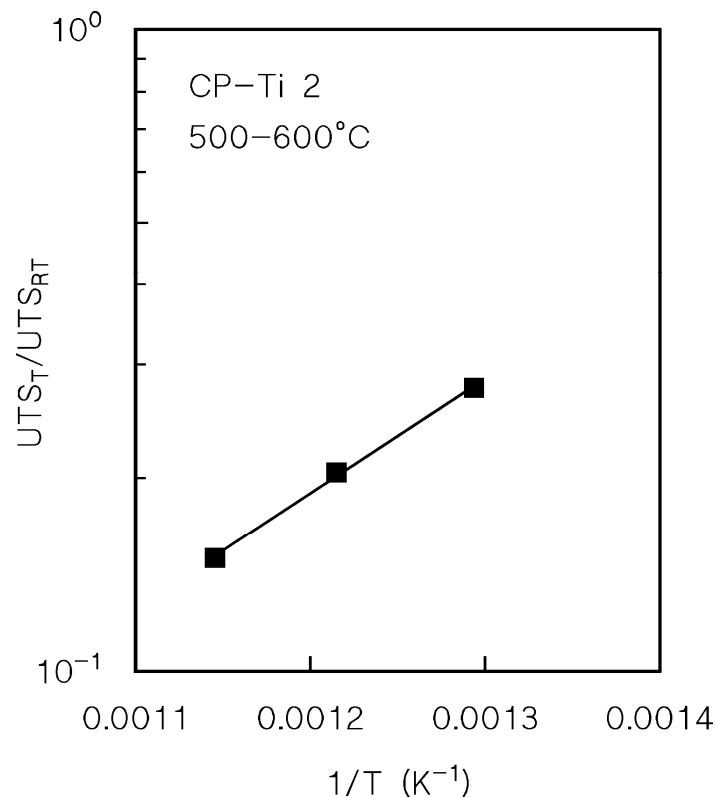


Figure 8. UTS_T data (experimental values at 500 and 600 and interpolated value at 550 °C from [32]) as a function of temperature, described by Equation (8).

The deviation of the experimental data from the model curves in the low-strain rate regime deserves a last comment. The analysis of oxidation effects during creep in air in [29] is convincingly demonstrated, in which for a sufficiently long time of exposure, small-sized samples, as those used in the present study, exhibit lower creep rates. This effect is due to the formation of a thin but very creep-resistant oxygen-rich layer that deforms under a similar creep rate to the softer sample interiors. This fact leads to a load-transfer effect, resulting in lower creep rates. This effect has been neglected here, but the discussion in [29] demonstrated that both the tests under 15 MPa at 550 °C and 600 °C were indeed affected by oxidation, resulting in minimum creep rates lower than those predicted by the model.

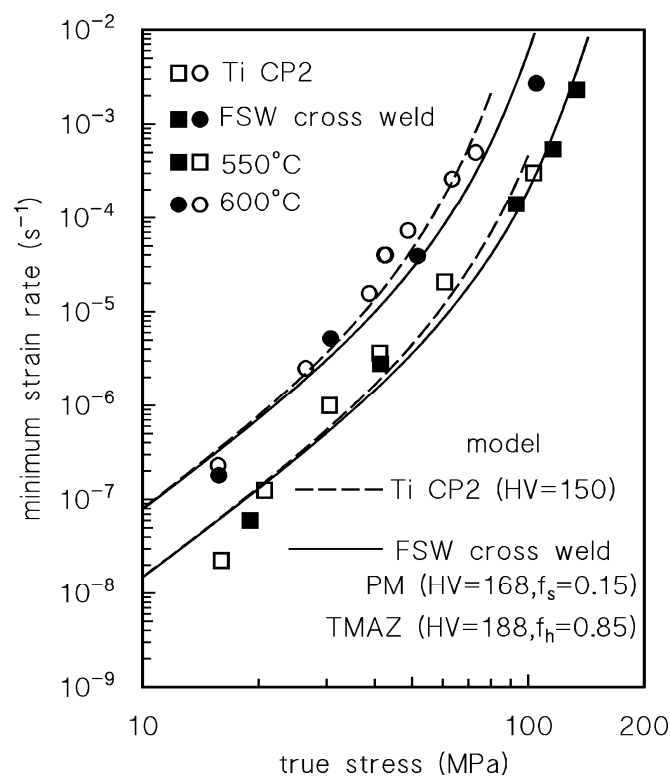


Figure 9. Minimum creep rate dependence on applied stress for Ti-CP 2 and for the FSW cross-weld samples and model curves.

5. Conclusions

The creep response of cross-weld (CW) samples of commercially pure Ti (grade 2) was investigated in the present study. The experimental results confirmed that the CW samples exhibited lower minimum creep rates when compared with parent metal (PM) ones. This effect was more evident in the high-stress region. Creep strain was indeed mainly localized in the softer portions of the specimen (base metal), while the thermo-mechanically affected zone (TMAZ), which was much harder, exhibited lower deformation. Based on these observations, the material was modeled as a composite, in which the hard TMAZ and the soft PM deform under the same applied stress. Constitutive equations recently developed to describe the minimum creep rate dependence on applied stress for Ti-CP 2 were used to estimate the creep response of the hard and soft zones. The resulting model curves provided a more than reasonable description of the minimum creep rate dependence on the applied stress of the CW samples. This is a remarkable result because the calculation of the model curves did not require any data-fitting of the creep data, just an estimation of the UTS and the volume fraction of the hard (TMAZ) portion of the sample.

Author Contributions: Conceptualization, S.S. and M.R.; methodology, S.S.; validation, S.S. and M.R.; formal analysis, S.S., A.S. and M.C.; investigation, S.S., E.S., M.C. and A.S.; resources, M.R.; data curation, A.S.; writing—original draft preparation, S.S. and E.S.; writing—review and editing, E.S.; visualization, S.S.; supervision, S.S.; project administration, S.S. and M.R.; funding acquisition, M.R. All authors have read and agreed to the published version of the manuscript.

Funding: This research project is partially funded by Braude College (Karmiel, Israel) internal researchers' grant.

Data Availability Statement: The data presented in this study are available on request from the corresponding author.

Acknowledgments: The assistance of N. Navot with welding the material and of A. Leccese in metallographic activities is highly appreciated.

Conflicts of Interest: The authors declare no conflict of interest.

References

1. Singh, R.P.; Dubey, S.; Singh, A.; Kumar, S. A review paper on friction stir welding process. *Mater. Today Proc.* **2021**, *38*, 6–11. [[CrossRef](#)]
2. Reshad Seighalani, K.; Besharati Givi, M.K.; Nasiri, A.M.; Behemat, P. Investigations on the effects of the tool material, geometry, and tilt angle on friction stir welding of pure titanium. *J. Mater. Eng. Perform.* **2010**, *19*, 955–962. [[CrossRef](#)]
3. Fujii, H.; Sun, Y.; Kato, H.; Nakata, K. Investigation of welding parameter dependent microstructure and mechanical properties in friction stir welded pure Ti joints. *Mater. Sci. Eng. A* **2010**, *527*, 3386–3391. [[CrossRef](#)]
4. Karna, S.; Cheepu, M.; Venkateswarulu, D.; Srikanth, V. Recent developments and research progress on friction stir welding of titanium alloys: An overview. *IOP Conf. Ser. Mater. Sci. Eng.* **2018**, *330*, 012068. [[CrossRef](#)]
5. Lee, W.B.; Lee, C.Y.; Chang, W.S.; Yeon, Y.M.; Jung, S.B. Microstructural investigation of friction stir welded pure titanium. *Mater. Lett.* **2005**, *59*, 3315–3318. [[CrossRef](#)]
6. Zhang, Y.; Sato, Y.S.; Kokawa, H.; Park, S.H.C.; Hirano, S. Stir zone microstructure of commercial purity titanium friction stir welded using pcBN tool. *Mater. Sci. Eng. A* **2008**, *488*, 25–30. [[CrossRef](#)]
7. Xu, N.; Song, Q.; Bao, Y.; Jiang, Y.; Shen, J.; Cao, X. Twinning-induced mechanical properties' modification of CP-Ti by friction stir welding associated with simultaneous backward cooling. *Sci. Technol. Weld. Join.* **2017**, *7*, 610–616. [[CrossRef](#)]
8. Bahl, S.; Nithilaksh, P.L.; Suwas, S.; Kailas, S.V.; Chatterjee, K. Processing–microstructure–crystallographic texture–surface property relationships in friction stir processing of titanium. *J. Mater. Eng. Perform.* **2017**, *26*, 4206–4216. [[CrossRef](#)]
9. Kang, D.S.; Lee, K.J. Recent R&D status on friction stir welding of Ti and its alloys. *J. Weld. Join.* **2015**, *33*, 1–7.
10. Liu, H.; Nakata, K.; Yamamoto, N.; Liao, J. Friction stir welding of pure titanium lap joint. *Sci. Technol. Weld. Join.* **2010**, *15*, 428–432. [[CrossRef](#)]
11. Fonda, R.W.; Knipling, K.E.; Levinson, A.J.; Feng, C.R. Enhancing the weldability of CP titanium friction stir welds with elemental foils. *Sci. Technol. Weld. Join.* **2019**, *24*, 617–623. [[CrossRef](#)]
12. Giri, S.R.; Kumar Khamari, B.; Moharana, B.R. Joining of titanium and stainless steel by using different welding processes: A review. *Mater. Today Proc.* **2022**, *66*, 505–508. [[CrossRef](#)]
13. Gadakh, V.S.; Badheka, V.J.; Mulay, A.S. Solid-state joining of aluminum to titanium: A review. *Proc. Inst. Mech. Eng. Part L* **2021**, *235*, 1757–1799. [[CrossRef](#)]
14. Patel, S.; Fuse, K.; Gangvekar, K.; Badheka, V. Multi-response optimization of dissimilar Al-Ti alloy FSW using Taguchi-Grey relational analysis. *Key Eng. Mater.* **2020**, *833*, 35–39. [[CrossRef](#)]
15. Pereira, V.F.; Fonseca, E.B.; Costa, A.M.S.; Bettini, J.; Lopes, E.S.N. Nanocrystalline structural layer acts as interfacial bond in Ti/Al dissimilar joints produced by friction stir welding in power control mode. *Scr. Mater.* **2020**, *174*, 80–86. [[CrossRef](#)]
16. Asmael, M.B.A.; Glaissa, M.A.A. Effects of rotation speed and dwell time on the mechanical properties and microstructure of dissimilar aluminum-titanium alloys by friction stir spot welding (FSSW). *Materwiss. Werksttech.* **2020**, *51*, 1002–1008. [[CrossRef](#)]
17. Elshaer, R.N.; Ibrahim, K.M. Applications of Titanium Alloys in Aerospace Manufacturing: A Brief Review. *Bull. TIMS* **2022**, *111*, 60–69. [[CrossRef](#)]
18. Choi, S.-W.; Jeong, J.S.; Won, J.W.; Hong, J.K.; Choi, Y.S. Grade-4 commercially pure titanium with ultrahigh strength achieved by twinning-induced grain refinement through cryogenic deformation. *J. Mater. Sci. Technol.* **2021**, *66*, 193–201. [[CrossRef](#)]
19. Nicholson, W.J. Titanium Alloys for Dental Implants: A Review. *Prosthesis* **2020**, *2*, 100–116. [[CrossRef](#)]
20. Chong, Y.; Poschmann, M.; Zhang, R.; Zhao, S.; Hooshmand, M.S.; Rothchild, E.; Olmsted, D.L.; Morris, J.W., Jr.; Chrzan, D.C.; Asta, M.; et al. Mechanistic basis of oxygen sensitivity in titanium. *Sci. Adv.* **2020**, *6*, eabc4060. [[CrossRef](#)]
21. Gardner, H.M.; Gopon, P.; Magazzeni, C.M.; Radecka, A.; Fox, K.; Rugg, D.; Wade, J.; Armstrong, D.E.J.; Moody, M.P.; Bagot, P.A.J. Quantifying the effect of oxygen on micro-mechanical properties of a near-alpha titanium alloy. *J. Mater. Res.* **2021**, *36*, 2529–2544. [[CrossRef](#)]
22. Texier, D.; Sirvin, Q.; Velay, V.; Salem, M.; Monceau, D.; Mazères, B.; Andrieu, E.; Roumiguier, R.; Dod, B. Oxygen/nitrogen-assisted embrittlement of titanium alloys exposed at elevated temperature. In Proceedings of the 14th World Conference on Titanium, Ti2019, Nantes, France, 10–14 June 2019.
23. Regev, M.; Almoznino, B.; Spigarelli, S. A Study of the Metallurgical and Mechanical Properties of Friction-Stir-Welded Pure Titanium. *Metals* **2023**, *13*, 524. [[CrossRef](#)]
24. Callegari, B.; Oliviera, J.P.; Aristizabal, K.; Coelho, R.S.; Brito, P.P.; Wu, L.; Schell, N.; Soldera, F.A.; Mucklich, F.; Pinto, H.C. In-situ synchrotron radiation study of the aging response of Ti-6Al-4V alloy with different starting microstructures. *Mater. Charact.* **2020**, *165*, 110400. [[CrossRef](#)]
25. Rosen, A.; Rottem, A. The Effect of High-Temperature Exposure on the Creep Resistance of Ti-6Al-4V Alloy. *Mater. Sci. Eng.* **1976**, *22*, 23–29. [[CrossRef](#)]
26. Ranganath, S.; Mishra, R.S. Steady state creep behaviour of particulate-reinforced titanium matrix composites. *Acta Mater.* **1996**, *44*, 927–935. [[CrossRef](#)]
27. Barboza, M.J.R.; Perez, E.A.C.; Medeiros, M.M.; Reis, D.A.P.; Nono, M.C.A.; Piorino Neto, F.; Silva, C.R.M. Creep behavior of Ti-6Al-4V and a comparison with titanium matrix composites. *Mater. Sci. Eng. A* **2006**, *428*, 319–326. [[CrossRef](#)]

28. Guo, Y.; Liu, G.; Jiao, T.; Hu, X.; Zhang, H.; Liu, M. Creep-fatigue damage behavior of a titanium alloy at room temperature: Experiments and modeling. *Int. J. Mech. Sci.* **2023**, *245*, 108135. [[CrossRef](#)]
29. Regev, M.; Santoni, A.; Spigarelli, S. Oxidation Effects on Short-Term Creep Response in Air of Commercially Pure Titanium (CP-2 Ti). *Metals* **2023**, *13*, 1275. [[CrossRef](#)]
30. Hickey, C.F., Jr. *Strength-Hardness Correlation for Titanium Alloys*; Technical Report No. WAL TR 405.22/1; Waterton Arsenal Laboratories: Watertown, MA, USA, 1961.
31. Perez, R.A.; Nakajima, H.; Dymont, F. Diffusion in α -Ti and Zr. *Mater. Trans.* **2003**, *44*, 2–13. [[CrossRef](#)]
32. Shahmir, H.; Pereira, P.H.R.; Huang, Y.; Langdon, T.G. Mechanical properties and microstructural evolution of nanocrystalline titanium at elevated temperatures. *Mater. Sci. Eng. A* **2016**, *669*, 358–366. [[CrossRef](#)]

Disclaimer/Publisher’s Note: The statements, opinions and data contained in all publications are solely those of the individual author(s) and contributor(s) and not of MDPI and/or the editor(s). MDPI and/or the editor(s) disclaim responsibility for any injury to people or property resulting from any ideas, methods, instructions or products referred to in the content.